

Unveiling Ancient Maya Settlements Using Aerial LiDAR Image Segmentation

Jincheng Zhang¹, William Ringle², and Andrew Willis¹

¹University of North Carolina at Charlotte, Charlotte, NC 28223 USA

²Davidson College, Davidson, North Carolina, USA

¹{jzhang72, arwillis}@charlotte.edu

²biringle@davidson.edu

Abstract

Manual identification of archaeological features in LiDAR imagery is labor-intensive, costly, and requires archaeological expertise. This paper shows how recent advancements in deep learning (DL) present efficient solutions for accurately segmenting archaeological structures in aerial LiDAR images using the YOLOv8 neural network. The proposed approach uses novel pre-processing of the raw LiDAR data and dataset augmentation methods to produce trained YOLOv8 networks to improve accuracy, precision, and recall for the segmentation of two important Maya structure types: annular structures and platforms. The results show an IoU performance of 0.842 for platforms and 0.809 for annular structures which outperform existing approaches. Further, analysis via domain experts considers the topological consistency of segmented regions and performance vs. area providing important insights. The approach automates time-consuming LiDAR image labeling which significantly accelerates accurate analysis of historical landscapes.

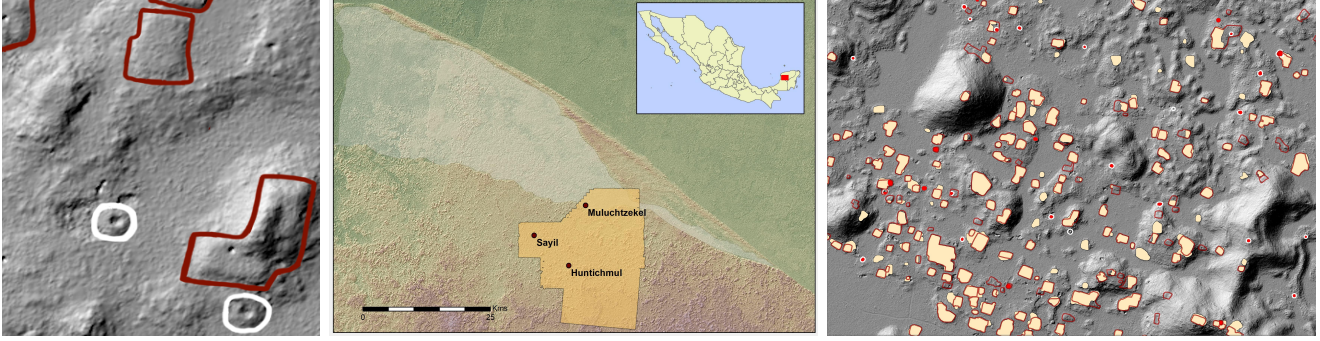
1 Introduction

Settlement archaeology attempts to determine the population of a past society and its disposition with respect to its surroundings. Sufficiently large samples of past landscapes have often been difficult to obtain because of dense vegetation and/or rugged terrain. However, starting in 2008, the introduction of LiDAR remote sensing technology to Maya archaeology allowed aerial coverage of hundreds of square kilometers within a few days [4, 5, 15, 19, 20, 23]. As a result, archaeologists now often face a surfeit of data, demanding the investment of many hours of skilled analysis. For example, over 60,000 house platforms were detected in LiDAR coverage of a large campaign across the lowlands of Guatemala [4]. As LiDAR coverage of the Maya low-

lands continues to expand, the burden of image analysis will increase dramatically, since the ancient population is estimated to have ranged into the millions.

The development of deep learning technologies has opened up vast possibilities for enhancing Maya settlement recognition within large LiDAR datasets, particularly through rapid object detection and segmentation techniques. Deep learning models can efficiently identify, classify, and segment objects of interest with high accuracy and speed. By leveraging these technologies, researchers can streamline the process of analyzing vast LiDAR datasets, enabling comprehensive surveys of Maya archaeological sites at a scale previously unattainable [1, 3, 7, 9, 18]. Moreover, deep learning facilitates the discovery of previously unnoticed objects and features, enriching the understanding of Maya civilization and cultural heritage.

This study explores the application of the state-of-the-art DL network YOLOv8 [10] for segmenting Maya structures found in the Puuc region of Yucatan, Mexico. The research focuses on two classes: (1) stone platforms supporting houses and other buildings, and (2) annular structures, circular mounds likely remnants of ancient pit kilns for lime production. Fig. 1a illustrated some examples of platforms and annular structures. Annular structures are usually about 10-12 m in diameter while stone platforms vary in size from a few meters to over a hundred meters, with most ranging from 200-1200 m². Training and evaluation of the deep learning system were conducted using objects of interest from three Puuc sites, Muluchtzekel (MLS), Sayil (SAY), and Huntichmul (HNT), as depicted in Fig. 1b. The LiDAR data of these sites were collected by the National Center for Airborne LiDAR and Mapping (NCALM) using a Teledyne Optech TitanMW(14SEN/CON340) sensor mounted in an airplane flying at an altitude of 600-650 m. From this, a 0.5 m resolution Digital Terrain Model (DTM) raster was produced where each pixel measures 0.5 meters in both width and height. To train YOLOv8 for Maya structure segmentation, LiDAR data were processed to generate image datasets



(a) Platforms and annular structures. (b) Location map of the Puuc region of Yucatan, Mexico. (c) Inference result on the Huntichmul site.

Figure 1: (a) Examples of platforms and annular structures visualized in a hillshading image where platforms are outlined in brown and annular structures are in white. (b) Maya structures found in three sites, Muluchtzekel (MLS), Sayil (SAY), and Huntichmul (HNT), in the Puuc region of Yucatan, Mexico were used as data for analysis. (c) The inference result of Huntichmul demonstrates the proposed system’s capability of extracting platforms and annular structures. The ground truth and predicted masks were superimposed onto a hillshading image for better visualization. The brown and white polygons respectively outline the ground truth boundaries of platforms and annular structures, while the solid beige and red regions show the predictions of YOLOv8 respectively.

of 256×256 pixels, using objects manually labeled and verified by ground surveying during the years 1984 - 2023.

The contributions of this article are:

- Identification of effective representations of aerial LiDAR data that best enhance segmentation results, incorporating archaeological evaluation metrics such as region topology for a more rigorous analysis than typically published.
- Development of novel pre-processing techniques for raw LiDAR data and dataset augmentation methods that maintain accuracy with a small training dataset.
- Introduction of a multi-scale inference approach and novel post-processing methods to improve the segmentation performance.
- Demonstration of performance across multiple archaeological sites, providing a comprehensive evaluation of the proposed methodology’s effectiveness.
- Discussion of end-user benefits of the system by a domain expert, detailing how the technology positively impacts large-scale survey annotation.
- Ablation studies examining the impact of different data representations and image scaling on segmentation performance, offering insights into key influencing factors.

The result of these contributions is the creation of a new system that automates the identification and segmentation of archaeological annular structures and platforms, demonstrating the immense potential of deep learning in streamlining labor-intensive tasks traditionally reliant on manual expertise.

2 Related Work

This section summarizes common data representations in imaging Maya structures, followed by recent developments in the segmentation of ancient Maya structures using deep learning networks.

2.1 ALS Raster Representations

Airborne Laser Scanning (ALS) is a powerful technique used in archaeology to create detailed 3D terrain models using laser pulses (LiDAR) gathered by an airborne sensor. For archaeological purposes, raw ALS point data are often converted to “bare earth” topographic models referred to as Digital Terrain Models (DTM). ALS raster data representations are the grayscale or color raster image representations derived from the DTM.

ALS raster data representations [12], including hillshading (HS), slope, sky-view factor (SVF), openness, etc, offer contrasting insights into terrain characteristics. HS provides a visually intuitive representation based on the assumption of a Lambertian surface (equally bright from all directions) [14] illuminated by a distant light source. The slope is the first derivative (gradient) of the surface elevation. SVF depicts the visible sky portion from a point, offering an alternative to hillshading to overcome the directional problem discussed below. Openness estimates horizon elevation angles within a defined radius, with positive openness (PO) being the mean zenith angle value.

Combining representations can provide additional insights. Visualization for Archaeological Topography (VAT)

Site	Overall Area (km^2)	Area Surveyed (km^2)	Hills (%)	Flats (%)	Low Rises (%)	Platforms	Annulars
MLS	6.00	4.03	0.172	0.081	0.747	564	61
SAY	12.00	3.14	0.127	0.021	0.852	646	112
HNT	4.50	1.04	0.243	0.061	0.696	513	70

Table 1: Ground survey statistics for three archaeological sites used in this paper. Areal statistics are followed by the distribution of terrain types, revealing that the landscapes of MLS and SAY have fewer hills when compared to HNT. “Hills” have a local height of 30 m or more, “Flats” have virtually no relief, and “Low Rises” comprise the remaining terrain. The last two columns show the number of manually identified platforms and annular structures.

is a widely used method, blending HS, slope, PO, and SVF representations. While VAT effectively shows the topographic features of archaeological sites and landscapes, its reliance upon hillshading makes it orientation-dependent. This limits its compatibility with data augmentation techniques like rotation and flipping [13], which are crucial for data processing in deep learning. An alternative combination was proposed in [18], creating a three-channel image representation using SVF, PO, and slope for DL classification tasks. This paper applies this representation to semantic segmentation and evaluates its effectiveness.

2.2 Segmentation on Archaeological Structures

Deep learning has emerged as a powerful tool for analyzing LiDAR and aerial imagery datasets in archaeological research, particularly in tasks like classification and semantic segmentation [2, 3, 7, 9, 11, 18]. Semantic segmentation involves accurately delineating architectural features within these datasets. Recent studies, such as those utilizing the U-Net architecture [16], have shown promising results, especially in identifying ancient Maya settlement features [1, 3, 9]. Other architectures like DeepLabv3 [6] and HR-Net [22] have also been explored in [11].

This article demonstrates methods that enable accurate segmentation of Maya platforms and annular structures using YOLOv8. To our knowledge, this neural architecture has not been applied to this application domain. The proposed methodology and results indicate the pre-processing steps needed to make YOLOv8 significantly outperform competing neural models.

3 Methodology

This section describes the DL model, how the data were conditioned for training the model, and how the trained model was applied to process large raw LiDAR data. The discussion is organized into the following sections:

- Data pre-processing steps that modify raw LiDAR data into measurements that yield higher performance.

- Data augmentation steps that expand the training database and yield higher performance.
- Inference processing methods that allow very large LiDAR images, for example, 3600×5000 , to be processed using a network having a 256×256 input layer and coping with tiling artifacts in the labeling.
- A brief overview of the DL model, YOLOv8.
- A summary of the evaluation approach including conventional pixel-based metrics and novel object-based topological metrics.

3.1 Dataset Pre-processing And Ground Truth

Table 1 presents statistics of the measured data and ground survey data for the three Puuc sites indicated in Fig. 1b. Significantly more platforms than annular structures are present in all three sites, with the former outnumbering the latter by approximately 6 to 9 times. This discrepancy in numbers can lead to data imbalance issues, where models trained on such datasets may exhibit biases favoring the majority class and consequently perform inadequately on minority classes. To address this concern, two distinct image datasets were generated: one specifically for platforms and another for annular structures.

The image for training and testing the network consists of three image channels: (1) SVF, (2) PO, and (3) Slope which we refer to as an SPS image (from the first letters of each channel) similar to work in [18]. The SPS image has the same resolution as the LiDAR DTM where each pixel spans 0.5 meters in width and 0.5 meters in height. This choice was motivated by the ablation study results which showed that SPS images yield better performance than other representations. Fig. 5 illustrated an SPS image tile and other ALS representations including SVF, PO, and slope.

The labeled SPS images, with sizes up to 6000×8000 , were divided into small tiles of 256×256 to generate the dataset for DL systems. Specifically, an image tile was created at the location of each object of interest with the tile center overlapping the object center.

Compared to image datasets of contemporary objects, the availability of ground-verified ancient Maya structures

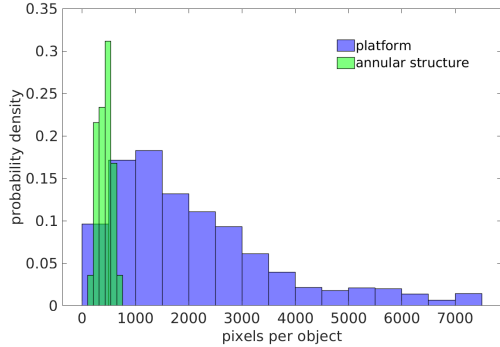


Figure 2: Pixel count per object for platforms and annular structures from the LiDAR images used in this paper.

is extremely limited, and collecting a large labeled dataset of them is challenging and expensive, hence the small sample sizes in Table 1. The ground truth labels of objects of interest were generated by superimposing georeferenced survey maps created between 1984 and 2023 on the LiDAR imagery (SAY data from [17], MLS and HNT by a domain expert). These were used to trace the outlines of house platforms and annular structures. Since mapping did not completely cover the regions of interest, objects of interest outside the surveyed area were traced manually using LiDAR imagery to provide sufficient data for training a deep learning system. Small structures invisible in the LiDAR imagery were excluded from ground truth labeling on the logic that similar structures identified by DL systems but invisible in the LiDAR imagery would be impossible to verify without further fieldwork. The ground truth labels were then exported as polygons enclosing each object.

3.2 Data Augmentation

The datasets present significant challenges for ML systems due to two attributes: (1) the small size of the label sets, and (2) the small size of labeled regions.

Due to the small size of the label sets, data augmentation was required to boost performance. The proposed augmentation approach adapted the methods in [9], including (1) random background sampling that collects random samples of background unrelated to the location of labeled objects, and (2) random rotations and translations of each training object. These methods virtually expand the dataset and improve data variation. However, translation during augmentation can move segmented structure regions to the image periphery and clip out significant portions of the structure data. When there is a very small extent of the structure in the augmented image, i.e., less than 10 pixels, the inclusion of the region label data adversely impacts segmentation since these data do not have sufficient pixels that can represent the features of objects. To address this, structures that are

clipped and possess bounding boxes smaller than 10 pixels in either width or height have their labels removed.

Augmentation of the datasets also included anisotropic scaling that scaled only (X, Y) dimensions of images by 2. Scaling the image can enlarge small objects and improve DL model performance. Fig. 2 shows the pixel count per object respectively for platforms and annular structures in the image data. Most objects are smaller than 3000 pixels, occupying less than 4.5% of a 256×256 image tile. This anisotropic approach is important to preserve the height (Z dimension) of the archaeological objects relative to their surroundings and the heights of objects, e.g., buildings, on platforms that do not typically scale with the platform (X, Y) footprint. Unlike conventional scaling approaches, we scale the SPS image at its captured resolution (on the order of 6000×8000) before dividing it into tiles, which has the impact of varying the perceptual field of each object.

Due to the diverse shapes of platforms compared to the mostly circular annular structures, which remain unchanged with rotation, the proposed pipeline generated 15 augmented variations at each scale for each platform object and 10 for each annular structure. The final realization of the augmented platform dataset comprises a total of 33,971 images, each sized at 256×256 pixels, while the annular structure dataset contains 3,216 images of the same dimensions.

3.3 Multi-Scale Inference and Post Processing

The proposed multi-scale approach performs inference on LiDAR image at its native resolution, i.e., each pixel is $0.25 m^2$, and a magnification of 2, i.e., each pixel is $0.125 m^2$. The magnified results are scaled down to the native resolution preserving positively labeled (X, Y) locations and merged with the lower resolution region using a logical OR of the results.

The final inference results are generated by post-processing the output from YOLOv8 to address two issues: (1) tiling artifacts created by partitioning very large raw LiDAR images in tiles for processing, and (2) removal of small segmented regions that are not likely to be of archaeological interest.

Tiling artifacts occur when structure boundaries are clipped before being input to the DL network. Segmentation for clipped objects often has incorrect linear boundaries that follow the tile boundary. As other researchers have done, a sliding window inference was applied for the image data which classifies the pixels multiple times for different window offsets. Each classification generates a segmentation mask and the logical OR of the generated masks across all windows generates the final segmentation result.

A review of the ground truth label set reveals that plat-

forms and annular structures have well-defined minimum area limits, 41 m^2 and 33 m^2 respectively, and only a small number of objects have areas close to these minimum thresholds. The proposed post-processing implements this prior knowledge to remove spurious small regions. Specifically, segmented output with bounding boxes smaller than 15 pixels (7.5 m) in either X or Y dimension were filtered out. This was achieved by a series of standard morphological operations.

3.4 YOLOv8 Deep Learning Architecture

YOLOv8 is the latest state-of-the-art YOLO (You Only Look Once) model that can be used for object detection, image classification, and instance segmentation tasks. The YOLOv8 segmentation model, as an extension of its detection model, makes use of a few key components to enhance the performance including (1) a CSPDarknet53 [21] feature extractor as the model backbone, (2) a novel C2f module as the model bottleneck that optimizes the traditional YOLO neck module for improving the model speed while maintaining similar performance, and (3) two segmentation heads that learn to predict the semantic segmentation masks for the input image. The YOLOv8 segmentation model has been shown to achieve state-of-the-art results on a wide variety of object detection and semantic segmentation benchmarks while maintaining high speed and efficiency.

3.5 Evaluation Metrics

This paper used a hybrid approach combining object-based and pixel-based metrics to assess segmentation performance. Object-based metrics assess segmentation success by measuring the intersections between predicted segment polygons and ground truth polygons. Pixel-based metrics assess the classification accuracy of individual pixels, including commonly used metrics such as IoU (Intersection over Union), Precision (P), and Recall (R). Throughout this article, true positives (TP), false positives (FP), and false negatives (FN) respectively refer to pixels correctly classified as belonging to the target class, pixels incorrectly classified as belonging to the target class, and pixels incorrectly classified as not belonging to the target class.

3.5.1 IoU

IoU, also known as the Jaccard Index, quantifies the overlap between the predicted pixels and the ground truth pixels for a target class. It ranges from 0 to 1, with higher values indicating better segmentation accuracy.

$$IoU = \frac{(\text{Prediction}) \cap (\text{Ground Truth})}{(\text{Prediction}) \cup (\text{Ground Truth})} \quad (1)$$

$$= \frac{TP}{TP + FP + FN}$$

3.5.2 Precision

Precision is the ratio of correctly predicted positive pixels to the total number of positive pixels. A high precision indicates that when the model predicts a positive pixel, it is likely to be correct. Precision is calculated by:

$$Precision = \frac{TP}{TP + FP} \quad (2)$$

3.5.3 Recall

Recall is the ratio of correctly predicted positive pixels to the total number of actual positive pixels. A high recall indicates that the model is effective at identifying all pixels of the positive class. Recall is calculated by:

$$Recall = \frac{TP}{TP + FN} \quad (3)$$

3.5.4 Object-based Metrics

Since the goal of segmentation is the identification of archaeological objects, a parallel series of object-based topological metrics were also developed to evaluate the inference results, which are perhaps more intuitively understood by non-DL specialists. The predicted masks of the inference data were converted to segmentation polygons for comparison with the ground truth polygons. The parity between the number of segmentation polygons and ground truth polygons provided a rough initial measure of success. Further analysis using GIS measured the intersections of segmentation polygons with ground truth polygons to evaluate segmentation success in a more detailed way. It was necessary to measure both the percentage of ground truth polygons intersecting inference polygons as well as the reverse since intersections were not always 1:1. That is, the areal overlap between a ground truth polygon and masks might be due to one or several mask polygons. Conversely, a given mask polygon might overlap several ground-truth polygons.

4 Results

This section discusses the segmentation results across the three archaeological sites, Muluchtzekel (MLS), Sayil (SAY), and Huntichmul (HNT) (Table 1, Fig. 3). Data from MLS and SAY were utilized for training and testing the YOLOv8 model, while data from HNT were used as

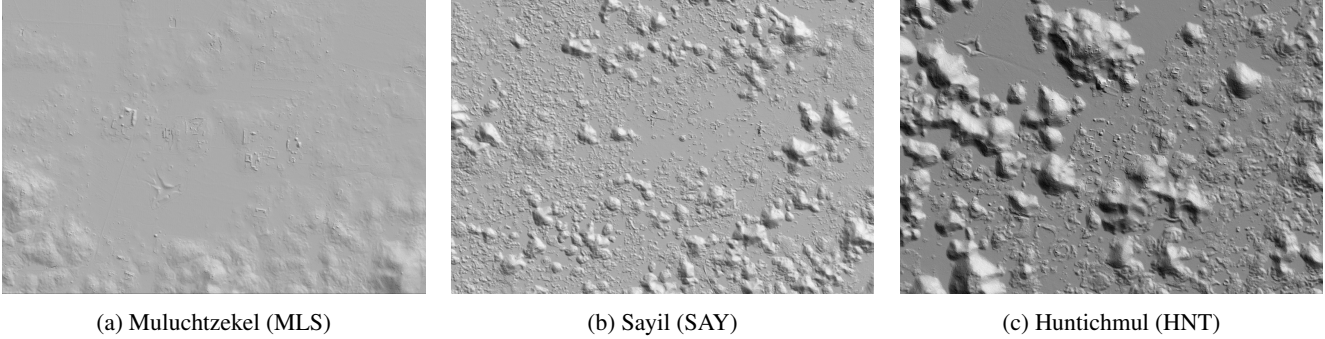


Figure 3: Hillshading image representation of MLS, SAY, and HNT sites where the "bumps" denote hill locations. The images of Muluchtzekel (MLS), Sayil (SAY), and Huntichmul (HNT) have a resolution of 6000×4000 , 6000×8000 , and 3600×5000 pixels respectively. The MLS and SAY sites are larger than the HNT despite being visualized in the same size.

inference data to assess the model’s effectiveness in a new site application. Performance improvements were realized as a combination of standard DL segmentation metrics, e.g., IoU, Recall, Precision, and a parallel GIS analysis. Ablation studies of this section demonstrate the performance impact of different pre-processing methods providing a best-practice recommendation.

Separate models were trained for platforms and annular structures. In both cases, computation was performed using an NVIDIA GeForce RTX 4090 GPU. The model to segment platforms was trained for 200 epochs with a batch size of 256. The model to segment annular structures was trained for 120 epochs also having batch size 256. No model parameters were fixed during training. Each dataset was divided into training (80%), validation (10%), and test (10%) sets. During the training process, the model was trained on the training set and validated on the validation set. Following the completion of training, the trained model underwent evaluation using the test set.

4.1 Testing on MLS and SAY

Table 2 shows the evaluation metrics for the trained model on the testing data. The YOLOv8 model trained for platform segmentation achieved an IoU performance of 0.842, with precision and recall rates exceeding 0.9. The annular structure model attained an IoU performance of 0.809, with precision and recall rates nearing 0.9. These results reflect high accuracy in locating and segmenting platforms and annular structures. The difference in performance between these two object types can be attributed to (1) the much smaller size of annular structures when compared to platforms, as shown in Fig. 2, making falsely segmented pixels have a relatively greater impact on the evaluation metrics for annular structures, and (2) the substantially fewer data instances in the annular structure dataset compared to the platform dataset, posing a challenge for the YOLOv8 model

		IoU	P	R
MLS & SAY (testing)	platform	0.842	0.902	0.926
	annular	0.809	0.891	0.898
HNT (inference)	platform	0.604	0.718	0.792
	annular	0.537	0.611	0.817

Table 2: Statistical results of the platform and annular structure segmentation on the testing set.

to learn features as effectively as it did for platforms. Thus, the overall performance on platforms benefits from distinct image features and a larger volume of training data than annular structures.

Previous research in ancient Maya structure segmentation had also reported results regarding platforms and, in one case, annular structures. The state-of-the-art performance includes achieving a 0.72 IoU score for platform segmentation on a dataset containing approximately 1900 platform samples from Petén, Guatemala [3], and a 0.765 IoU score on a dataset consisting of 952 image tiles, each containing at least one platform from Chactún, Mexico [1]. Additionally, authors in [9] reported an IoU score of 0.74 for platform segmentation and 0.82 for annular structures in their validation set. Due to the unavailability of these Maya datasets, direct comparison with our work is not possible at this time. However, the results of our study indicate that the proposed pre-process, data augmentation and post-processing techniques can contribute to improving performance for both platforms and annular structures.

4.2 Inference on HNT

Table 2 shows the evaluation metrics for the trained model on a third site, Huntichmul (HNT), that contains 513 platform targets and 70 annular structures. The overall IoU score was 0.604 for platform segmentation and 0.537 for

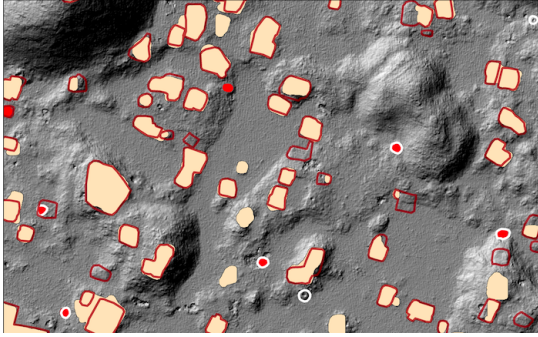


Figure 4: An excerpt of the inference result of HNT where the brown and white polygons respectively indicate the ground truth boundaries of platforms and annular structures and the solid beige and red regions respectively show the predictions of YOLOv8.

the annular structure, both having an approximately 0.25 decrease from the performance on the MLS and SAY sites. The precision and recall results shared a similar decrease as IoU. One possible explanation for this difference in performance could be the relatively smoother terrain (more flats and low rises) present in the training data (MLS and SAY) compared to the inference data (HNT), as indicated by the distribution of terrain types in Table 1. The performance of HNT may be improved by incorporating additional training samples from rugged terrain.

Figures 1c and 4 illustrate excerpts of the inference results obtained from HNT. Fig. 1c offers a broader field of view, while Fig. 4 provides a closer view, allowing for a more detailed examination of the results. The segmentation results showcase success in accurately identifying the majority of the objects, with failures primarily observed on smaller targets.

4.3 Topology Analyses of HNT Results

Table 3 presents the results of the object-based topology analyses. Approximately 83% of platform and annular ground truth polygons intersected an inference polygon, while 79.5% of platform and 70.7% of annular segmentation polygons intersected ground truth polygons, the difference perhaps attributable to the underproduction of inference platforms and overproduction of inference annular structures.

Table 4 divides intersection successes into quartiles based on the area of the ground truth polygons. This shows a clear contrast between the high number of failures in the lowest quartile, with less than 60% successful, with the very robust statistics of the upper three quartiles, with average success rates of 91.4% for platforms and 94.1% for annular structures. Reasons for the failure of small polygons to

		Total polygons	Intersects	Pct.
platform	GT	513	426	0.830
	pred	478	380	0.795
annular	GT	70	58	0.829
	pred	82	58	0.707

Table 3: The percentage (Pct.) of intersections of the ground truth (GT) and YOLOv8 predicted polygons from HNT respectively in the ground truth (GT) and YOLOv8 predicted polygons.

		Quartile	Max. Area (m^2)	Intersect Pct.
platform		1	210.7	0.581
		2	359.5	0.852
		3	633.3	0.906
		4	5700.3	0.984
		overall	5700.3	0.830
annular		1	74.0	0.500
		2	103.6	0.882
		3	125.5	0.941
		4	238.2	1.0
		overall	238.2	0.829

Table 4: Percentages of the HNT segmented polygons that intersect the ground truth polygons. The ground truth polygons were sorted by area and divided into quartiles to investigate where failures were occurring.

segment correctly include (1) their resemblance to natural features, (2) the "bumpiness" of the LiDAR data, and (3) the small number of pixels involved.

4.4 Ablation Studies

This section provides results for two ablation studies that investigate the effectiveness of (1) the SPS representation of the data compared to other representations and (2) the impact of multi-scale methods for training and inference on our data. Both studies evaluate performance using the platform dataset which has more samples and therefore can be expected to yield more accurate results for these studies. We feel that the conclusions drawn from the ablation studies generalize across segmentation tasks for other objects within the dataset.

4.4.1 Airborne LiDAR Data Representation

Table 5 presents the performance of platform segmentation using different ALS data representations derived from the DTM. The elevation data within each training tile was normalized to the $[0, 1]$ interval, a practice known to enhance classification outcomes, as corroborated by prior studies

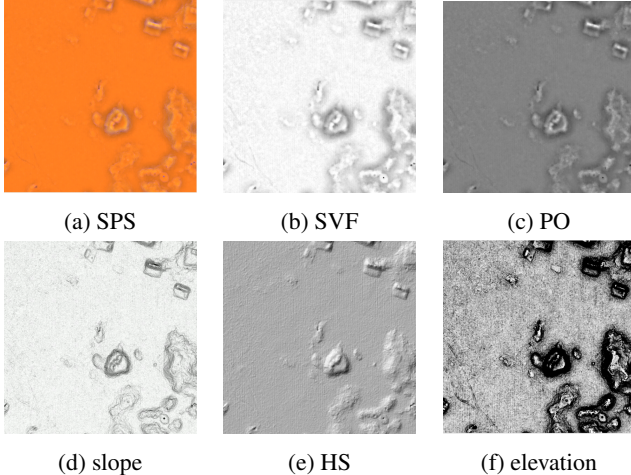


Figure 5: Different ALS data representations.

[8, 9]. Examples of these representations are depicted in Fig. 5. To create three-channel data for training input, the single-channel slope, PO, SVF, HS, and elevation data were replicated across the remaining two channels.

	IoU	P	R
SPS	0.842	0.902	0.926
SVF	0.832	0.899	0.917
PO	0.838	0.903	0.923
slope	0.823	0.901	0.905
HS	0.834	0.901	0.918
elevation	0.812	0.889	0.904

Table 5: Statistical testing results of platform segmentation from using different ALS data representations.

As indicated in Table 5, employing SPS yields better results in terms of IoU score and recall rate, ranking second in precision rate with a marginal difference of 0.001 from the top performer. SPS, a composite of the slope, PO, and SVF data, offers richer information compared to individual data components, potentially furnishing more discernible features for DL networks to exploit. On the other hand, employing elevation data and slope data (the first gradient of elevation) trails behind in all three metrics, suggesting that elevation data alone may not suffice for a deep learning system to effectively learn the segmentation of Maya structures. While hillshading and elevation representations may seem visually appealing to the eye and could provide researchers with an intuitive understanding when examining archaeological sites, this does not necessarily translate to improved performance for DL segmentation models.

4.4.2 Multi-scale

Table 6 shows the performance of testing and inference when incorporating multi-scale methods images into data augmentation training and inference post-processing. Two networks were trained: one with scaling the training data (“*HNT w/o scaling*”) and the other without scaling (“*train w/o scaling*”). These networks were evaluated in three scenarios: (1) on the test set with the same scaling factor as the training set (“*test w/ scaling*” and “*test w/o scaling*”), (2) on inferring the HNT image (“*HNT w/o scaling*”), and (3) on inferring a combination of the HNT image and its scaled variant (“*HNT w/ scaling*”) using the approach described in Section 3.3.

As demonstrated in Table 6, the best testing outcomes are observed when the training data incorporate scaled data. Similarly, the best inference results occur when the network is trained with scaled data and applied to infer the HNT combination. Overall, the results in “*HNT w/o scaling*” are better than those in “*train w/o scaling*”. Notably, scaling the HNT image leads to a notable improvement in inference performance, enhancing results by approximately 8% for both networks trained with and without scaled data.

5 End-user Benefits

The benefits of image segmentation for the archaeologist are clear. Manual identification of platforms in a large LiDAR dataset can cost weeks or months of dedicated analyst time. Consistency in identification may also be an issue, and with larger datasets, there is rarely the luxury of full re-analysis. Platform polygons vary tremendously in their footprints, while small natural undulations in the terrain can easily be mistaken for construction. Thus, image segmentation provides the end-user with a rapid and consistent initial pass through the LiDAR dataset, providing reliable identifications for a high proportion of the larger structures. Human analysts can then devote added time to smaller and more ambiguous features.

		IoU	P	R
train w/ scaling	test w/ scaling	0.842	0.902	0.926
	HNT w/o scaling	0.559	0.804	0.647
	HNT w/ scaling	0.604	0.718	0.792
train w/o scaling	test w/o scaling	0.83	0.894	0.921
	HNT w/o scaling	0.549	0.807	0.632
	HNT w/ scaling	0.591	0.741	0.745

Table 6: Statistical testing and HNT inference results of platform segmentation when applying different scale factors to generating the training data.

As to the ability of segmentation to accurately determine

platform outlines, the results are often remarkably close to what a human observer would posit. Given the variety of footprints, however, it is probably premature to invest too much faith in their accuracy. Human analysts will be able to accept many segmentation masks but will also need to manually adjust a substantial percentage.

6 Conclusion

This study automates the identification and segmentation of archaeological structures, such as annular structures and platforms, showcasing the immense potential of deep learning in streamlining labor-intensive tasks traditionally reliant on manual expertise. By introducing a novel data processing pipeline and achieving state-of-the-art segmentation performances, this research not only pushes the boundaries of deep learning applications in archaeology but also addresses the unique challenges posed by aerial LiDAR data. The utilization of YOLOv8 not only enhances the accuracy of archaeological structure segmentation but also presents a promising avenue for the automated analysis of vast archaeological landscapes. As these deep learning technologies continue to advance, their potential to revolutionize Maya object recognition in large LiDAR datasets is increasingly evident, promising new insights and discoveries that contribute to the broader field of archaeology.

Acknowledgments

We would like to acknowledge funding for LiDAR acquisition from the National Science Foundation (Award No. 1660503) and the National Center for Airborne LiDAR Mapping for the collection of the data used in this article.

References

- [1] Christian Ayala, Carlos Aranda, and Mikel Galar. A deep learning approach to ancient Maya architectures detection using aerial laser scanning data. *Publishers Jožef Stefan Institute, Jamova cesta 39, 1000 Ljubljana, Slovenia*, page 21, 2022.
- [2] Paweł Zbigniew Banasiak, Piotr Leszek Berezowski, Rafał Zapłata, Miłosz Mielcarek, Konrad Duraj, and Krzysztof Stereńczak. Semantic segmentation (u-net) of archaeological features in airborne laser scanning—example of the białowieża forest. *Remote Sensing*, 14(4):995, 2022.
- [3] Marek Bundzel, Miroslav Jaščur, Milan Kováč, Tibor Lieskovský, Peter Sinčák, and Tomáš Tkáčik. Semantic segmentation of airborne lidar data in Maya archaeology. *Remote Sensing*, 12(22):3685, 2020.
- [4] Marcello A Canuto, Francisco Estrada-Belli, Thomas G Garrison, Stephen D Houston, Mary Jane Acuña, Milan Kováč, Damien Marken, Philippe Nondédéo, Luke Auld-Thomas, Cyril Castanet, et al. Ancient lowland Maya complexity as revealed by airborne laser scanning of northern Guatemala. *Science*, 361(6409):eaau0137, 2018.
- [5] Arlen F Chase, Diane Z Chase, John F Weishampel, Jason B Drake, Ramesh L Shrestha, K Clint Slatton, Jaime J Awe, and William E Carter. Airborne lidar, archaeology, and the ancient Maya landscape at Caracol, Belize. *Journal of Archaeological Science*, 38(2):387–398, 2011.
- [6] Liang-Chieh Chen, George Papandreou, Florian Schroff, and Hartwig Adam. Rethinking atrous convolution for semantic image segmentation. *arXiv preprint arXiv:1706.05587*, 2017.
- [7] Thorben Hellweg, Stefan Oehmcke, Ankit Kariryaa, Fabian Gieseke, and Christian Igel. Ensemble learning for semantic segmentation of ancient maya architectures. *Publishers Jožef Stefan Institute, Jamova cesta 39, 1000 Ljubljana, Slovenia*, page 13, 2022.
- [8] Maroš Hliboký, Marek Bundzel, and Stanislav Husár. Detecting ancient Mayan construction activity by U-Net. In *2022 IEEE 20th Jubilee World Symposium on Applied Machine Intelligence and Informatics (SAMII)*, pages 000231–000236. IEEE, 2022.
- [9] Fatema-E Jannat, Jincheng Zhang, Andrew Willis, and William Ringle. Extracting ancient Maya structures from aerial lidar data using deep learning. In *SoutheastCon 2023*, pages 295–302. IEEE, 2023.
- [10] Glenn Jocher, Ayush Chaurasia, and Jing Qiu. Ultralytics YOLO, 2023.
- [11] Dragi Kocev, Nikola Simidjievski, Ana Kostovska, Ivica Dimitrovski, and Žiga Kokalj. Discover the mysteries of the maya: Selected contributions from the machine learning challenge & the discovery challenge workshop at ecml pkdd 2021. *arXiv preprint arXiv:2208.03163*, 2022.
- [12] Žiga Kokalj and Ralf Hesse. *Airborne laser scanning raster data visualization: a guide to good practice*. Založba ZRC, 2017.
- [13] Žiga Kokalj, Sašo Džeroski, Ivan Šprajc, Jasmina Štajdohar, Andrej Draksler, and Maja Somrak. Machine learning-ready remote sensing data for Maya archaeology. *Scientific Data*, 10(1):558, 2023.
- [14] Michael Oren and Shree K Nayar. Generalization of Lambert’s reflectance model. In *Proceedings of the 21st annual conference on Computer graphics and interactive techniques*, pages 239–246, 1994.
- [15] William M Ringle, Tomás Gallareta Negrón, Rossana May Ciau, Kenneth E Seligson, Juan C Fernandez-Diaz, and David Ortegón Zapata. Lidar survey of ancient maya settlement in the Puuc region of Yucatan, mexico. *PLoS One*, 16(4):e0249314, 2021.
- [16] Olaf Ronneberger, Philipp Fischer, and Thomas Brox. U-net: Convolutional networks for biomedical image segmentation. In *Medical Image Computing and Computer-Assisted Intervention—MICCAI 2015: 18th International Conference, Munich, Germany, October 5-9, 2015, Proceedings, Part III 18*, pages 234–241. Springer, 2015.
- [17] Jeremy A. Sabloff and Gair Tourtellot. *The Ancient Maya City of Sayil: The Mapping of a Puuc Region Center*. Middle American Research Institute, Pub. 60. New Orleans, 1991.

- [18] Maja Somrak, Sašo Džeroski, and Žiga Kokalj. Learning to classify structures in ALS-derived visualizations of ancient Maya settlements with CNN. *Remote Sensing*, 12(14):2215, 2020.
- [19] Ivan Šprajc, Aleš Marsetič, Jasmina Štajdohar, Sara Dzul Góngora, Joseph W Ball, Octavio Esparza Olguín, and Žiga Kokalj. Archaeological landscape, settlement dynamics, and sociopolitical organization in the Chactún area of the central Maya Lowlands. *Plos one*, 17(1):e0262921, 2022.
- [20] Travis W Stanton, Traci Ardren, Nicolas C Barth, Juan C Fernandez-Diaz, Patrick Rohrer, Dominique Meyer, Stephanie J Miller, Aline Magnoni, and Manuel Pérez. ‘structure’ density, area, and volume as complementary tools to understand Maya settlement: An analysis of lidar data along the great road between Coba and Yaxuna. *Journal of Archaeological Science: Reports*, 29:102178, 2020.
- [21] Chien-Yao Wang, Hong-Yuan Mark Liao, Yueh-Hua Wu, Ping-Yang Chen, Jun-Wei Hsieh, and I-Hau Yeh. CSPNet: A new backbone that can enhance learning capability of CNN. In *Proceedings of the IEEE/CVF conference on computer vision and pattern recognition workshops*, pages 390–391, 2020.
- [22] Jingdong Wang, Ke Sun, Tianheng Cheng, Borui Jiang, Chaorui Deng, Yang Zhao, Dong Liu, Yadong Mu, Mingkui Tan, Xinggang Wang, et al. Deep high-resolution representation learning for visual recognition. *IEEE transactions on pattern analysis and machine intelligence*, 43(10):3349–3364, 2020.
- [23] Jason Yaeger, M Kathryn Brown, and Bernadette Cap. Locating and dating sites using lidar survey in a mosaic landscape in western Belize. *Advances in Archaeological Practice*, 4(3):339–356, 2016.